5
Graphite Coated Ni Core-Shell Nanomaterial and its Composites for 12.4-18 GHz MW Absorption

5.1 INTRODUCTION

Recently, nanomaterials attracted their interest for MW absorbing applications due to their high surface to volume ratio at reduced size, providing enhanced un-saturated/dangling chemical bonds /sites causing interfacial polarization and scattering sites for incident MW radiation [Wang *et al*., 2011; Zhou *et al.*, 2007]. Further, these materials also offer opportunity to adjust the EM properties at reduced weight penalty for application on airborne platforms [Cao *et al.*, 2009]. The research on nanomaterials based MW absorbers was earlier focusing mainly on nano-ferrites, nano-metals, nano-alloys, carbonaceous nanomaterials etc. [Liao *et al.*, 2010]. The core-shell structured materials with nanometal core embedded in dielectric shell have shown potential geometrical effect to demonstrate effective MW absorption properties at lower absorber thickness [Zhang *et al.*, 2014; Sharma *et al.*, 2009; Xiao *et al.*, 2006]. At high frequencies, particularly in GHz range, permeability of metallic particles decreases due to the onset of eddy currents under the influence of external microwave radiation [Tang *et al.*, 2004; Zhao *et al.*, 2004]. This problem of eddy currents can be avoided by restricting the size of magnetic materials within the limit of skin depth of materials, corresponding to the incoming EM radiation. The skin depth ($\delta_m = 1/\sqrt{\pi f \mu \sigma}$) of EM wave inside materials depend on EM frequency (f), permeability of material (μ) and conductivity of materials (σ). Therefore, the nano-metals with particle size in the range of 1-50 nm inside the dielectric shell to isolate the individual metallic particles may provide the solution for such problem. The dielectric shell may also improve the magnetic stability by reducing the random flipping of the magnetic moment because of thermal fluctuations in conjunction with oxidation and corrosion protection for the metallic core. These materials in core/shell geometries provide the co-operative effects for MW absorption, relying on the nature and structure of magnetic metallic core and dielectric shell.

The frequency dispersive characteristics of permittivity for metallic core systems is attributed to the two kinds of polarization mechanisms under the influence of external EM field i.e. space-charge polarization and dipolar polarization. The interfacial/space charge polarization between neighboring conductive metal particles gives rise to the high dielectric constant for such systems [Kim *et al.*, 2004]. However, metal particles embedded in an insulated/conductive matrix, the space charge polarization appears at the interfaces of metal and insulator/conductive shell, as shown in Figure 5.1. The charge accumulation at the metal-shell interface is contributed by free electrons from the metallic core, enhancing the conductivity and thus, higher permittivity for the core/shell geometrical systems. Once the MW radiation has penetrated inside graphitic shell, it loses its energy through relaxation of space charge polarization. This space charge induced loss mechanic is effective at relatively lower MW frequency range. Further, the dipole polarization in core-shell metal nanoparticles is responsible for MW loss at higher MW frequency range. In the case of magnetic core, the loss of MW energy is due to spin resonance relaxation. Moreover, the graphitic shell also plays a major role in MW absorption loss through conduction loss mechanism. Therefore, in core-shell structures, the total MW absorption (A_T) is given by $A_T = A_P + A_\mu + A_\varepsilon$, where A_μ is MW absorption due to high permeability of magnetic core, A_P is MW absorption due to relaxation of dipolar and interfacial polarization and A_ε is dielectric losses due

to shell layer. However, estimating the contribution of individual component from the total MW absorption contribution is quite complex.

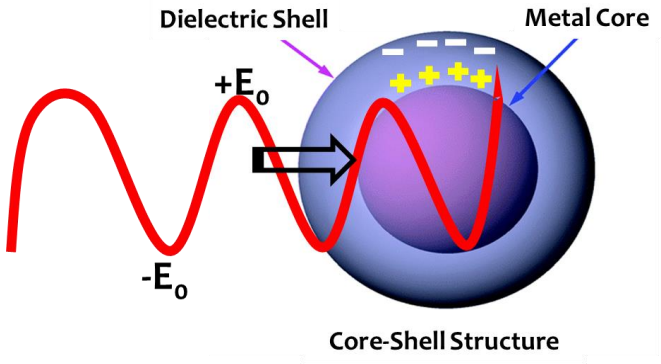

Figure 5.1 : Origin of interfacial polarization in core-shell structures

Several techniques have been employed for synthesizing carbon-coated metal nanocrystallites, such as carbon arc technique [Scott and Majetich, 1995], magnetron and ion-beam co-sputtering [Delaunay *et al.*, 1997], chemical vapor deposition [Sano *et al.*, 2003] and laser pyrolysis [Bi *et al.*, 1993]. In most of these techniques, the major drawback is the poor yield of the final product and high processing cost. In the present study, attempts have been made to synthesize the graphite coated Ni nanoparticles under the controlled pyrolytic annealing conditions as well as used them for synthesizing the rubber composites for MW absorption. The process consists of (i) Preparation of Ni $(OH)_2$ nanocomposites in copolymer matrix (ii) Conversion of Ni nanoparticles core by restricted heat treatment in inert condition (iii) Optimizing conditions for conversion of carbon shell into graphitic form, and (iv) Processing them in to rubber composites. The finally prepared rubber composite samples are studied for reflection loss characteristics as a function of thickness of rubber composite sheets. The reported synthetic route is simple, cost effective and scalable to produce the desired material for MW absorption applications.

5.2 EXPERIMENTAL PROCEDURE

As a typical synthesis, initially 10ml of (0.1M) of aniline was mixed with 50ml of distilled water and added 12 ml (0.1 M) of concentrate hydrochloric acid (HCl), which resulted into the formation of water soluble aniline hydrochloride. After that, 10 ml (0.1 M) of formaldehyde (HCHO) was added to the mixture. The solution was kept for 1h to cool down to the room temperature. Simultaneously, salt solution of 0.1M solution of nickel chloride ($NiCl_2$) was prepared separately by dissolving Ni salt in distilled water. This solution was then slowly added to the pre-cooled copolymer solution with continuous stirring. This entire mixture was added into 10% sodium hydroxide solution (NaOH) and stirred for 10-15 minutes for homogenization. The resulted precipitate was then filtered under vacuum and washed with the hot distilled water till the filtered solution became free from alkali metal ions. The precipitate was then dried in oven at 40-45°C to get the nanocomposite powder, which is named as N_1 hereafter. The as prepared powder material was heat treated at elevated temperatures i.e. 550°C, 700°C and 850°C under high purity nitrogen atmosphere (~99%) for 1h and these samples are named as N_2, N_3 and N_4 respectively, hereafter. The schematics, describing the conversion of Ni nano-core and graphitic shell from Ni hydroxide polymer nanocomposite is shown in Figure 5.2.

The synthesized materials were characterized for structural, magnetic, morphological and MW characterizations. The sample N_4 showed the maximum saturation magnetization (M_s) and has been used for fabrication of rubber based composites. Rubber composites were fabricated by varying the loading fraction of N_4 powder from 50 to 75wt% in rubber matrix, as per details summarized in Table 5.1. The rubber based composites could not be fabricated beyond 75 wt% loading of N_4 powder, as composite sample became highly brittle. The EM parameters of rubber

composites were measured using wave guide transmission line technique in Ku-band (12.4-18 GHz) of MW spectrum. Based on the measured EM parameters, reflection loss (R.L.) values were calculated for all these composites samples.

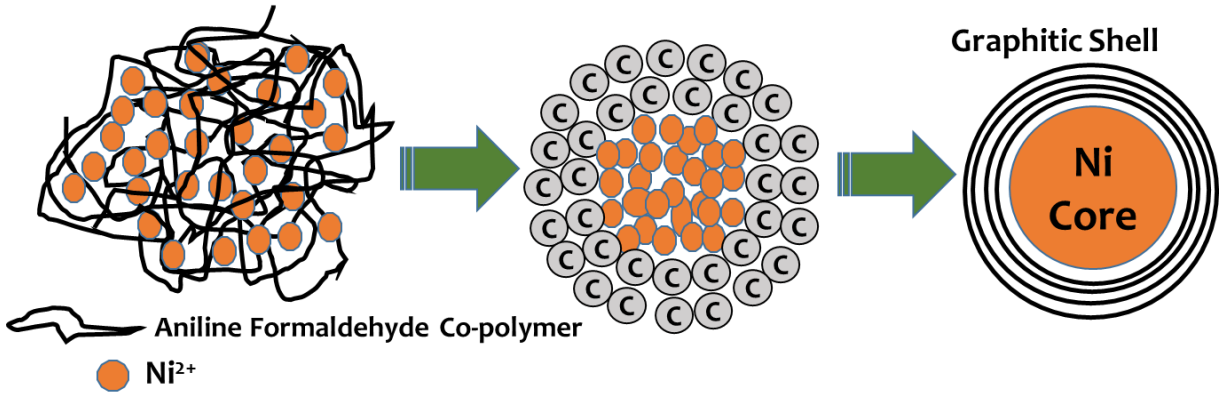

Figure 5.2: Schematic for formation of graphite coated core-shell structure

Table 5.1 : List of sample N4 loaded rubber composites

S. No.	Sample Code	Quantity of NBR (g)	Wt% of N_4 powder in rubber compound	Quantity of N_4 powder (g)	Enhancement in filler loading as compared to sample NIBR50 (x)
1.	NIBR40	10	40	6.7	0.67
2.	NIBR50	10	50	10	1.00
3.	NIBR60	10	60	15	1.50
4.	NIBR70	10	70	23.3	2.33
5.	NIBR75	10	75	30	3.00

5.3 RESULTS AND DISCUSSIONS

5.3.1 X-ray Diffraction Analysis

The XRD spectra of as prepared and annealed samples are shown in Figure 5.3. The broad diffraction peaks for N_1 sample are observed at 2θ values 18.2°, 33.04°, 38.2° and 59.0° correspond to (001), (100), (101) and (110) planes respectively for hexagonal $Ni(OH)_2$ structure (ICDD No. 14-0117), suggesting the presence of metal hydroxides. However, XRD spectra of N_2 sample, annealed at 550°C showed sharped (111), (200) and (220) diffraction planes, corresponding to the cubic Ni structure. Further, sample N_3, heat treated at higher temperature ~700°C showed additional diffraction peak at angle 26°, which correspond to the graphite hexagonal (002) diffraction plane, in conjunction with the observed cubic Ni crystallographic planes. The sample N_4, annealed at higher temperature ~850°C, is also showing the cubic Ni crystallographic structure with enhanced intensity of (002) graphite diffraction peaks, indicating the relatively enhanced crystallization of the graphitic carbon phase in these core-shell structures. These results indicate that formation of graphite phase along with Ni cubic metal phase at or above ~ 700°C annealing temperatures under nitrogen atmosphere. The broadening of Ni characteristics diffraction peaks has decreased with increase in the annealing temperature, indicating the larger grain growth of Ni nanoparticles.

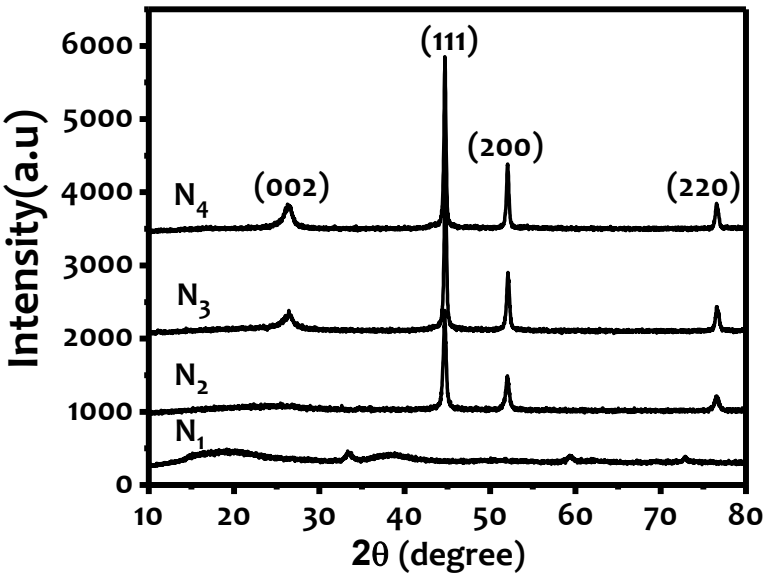

Figure 5.3: XRD pattern of samples N_1, N_2, N_3 and N_4

5.3.2 FTIR Analysis

Figure 5.4 shows FTIR spectra of as prepared and heat treated samples. The all peaks observed in case of as prepared sample N_1 are listed in Table-5.2. The absorption peak appeared at 3400 cm^{-1} is mainly due to N-H vibration and suggests the presence of secondary amino group in as prepared sample [Chiang and Mac Diramid, 1986]. This is consistent with the XRD observations, as explained in previous section. The other absorption peaks at 1595 cm^{-1} and 1516 cm^{-1} correspond to the quionoid ring and benzenoid ring respectively. Another strong absorption peak appeared at 1384 cm^{-1} is attributed to C-H in plane bending, may be coming from un-burnt reactants [Pant *et al.*, 2008]. The small absorption peaks observed at 3009 cm^{-1} and 830 cm^{-1} are appearing due to C-H stretching vibration and C-H out of plane wagging of 1,4-di-substituted benzene ring [Bellamy, 1975]. But in case of ~550°C annealed sample (N_2), only two absorption peaks at 1384 cm^{-1} and 830 cm^{-1} are observed. Further, intensity of these two peaks has decreased with increase in annealing temperature and completely reduced for 850°C heat treated N_4 sample. This suggests that polymer has been decomposed resulting the formation of graphite coated Ni-metal particle after heating at 850°C under nitrogen environment.

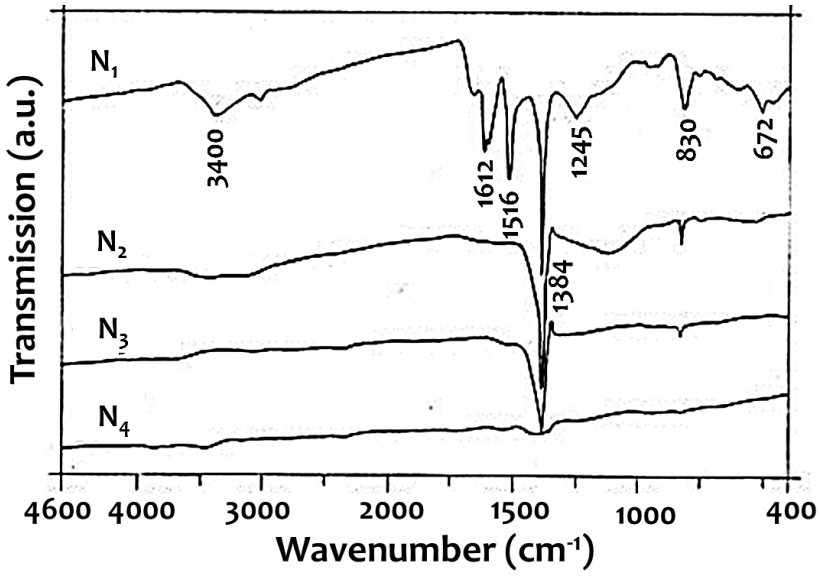

Figure 5.4: FTIR pattern of samples N_1, N_2, N_3 and N_4

Table-5.2: Identified FTIR modes of vibration and corresponding wavenumber

Peak Position (cm^{-1})	Mode of Vibration
672	Not Identified
830	C-H out of plane wagging of 1,4 disubstituted benzene ring
1245	C-N stretching
1384	C-H in plane bending
1516	C=C benzenoid ring
1595	C=C Quininoid ring
1612	C-H bending vibration of of 1,4 di-substituted benzene ring
1655	C=C stretching (aromatic)
3009	C-H stretching of benzene ring
3400	N-H stretching

5.3.3 TEM Studies

TEM studies on these samples have shown some interesting observations explaining the formation of nanoparticles of inorganic hydroxide embedded in the copolymer matrix. Figure 5.5 (a) shows the well dispersed inorganic hydroxide particles (darker part), embedded in polymer matrix (lighter part) and well attached with each other. This is in accordance with the observed XRD and FTIR measurements for as synthesized sample N_1. The TEM picture of 550°- 850°C heat treated samples (N_2-N_4) show the formation of nearly spherical nanoparticles as core in conjunction with graphitic carbon shell of sizes ~15nm, ~30nm and ~40 nm, respectively (Fig. 5.5b-d). The high resolution TEM (HRTEM) image of the same material is shown in Figure 5.6. The formation of Ni nano-core coated with graphitic shells can be observed clearly from the HRTEM image. This graphitic shell coating is possible with metallic core because of metal hydroxide particles encapsulation in the polymer host matrix, and its reduction under reducing environment at elevated temperatures. Moreover, the observation of broad (002) diffraction peak of graphitic carbon phase in XRD spectra as compared to Ni diffraction peaks suggests the formation of thin layer of graphite shell over Ni metal nanoparticles.

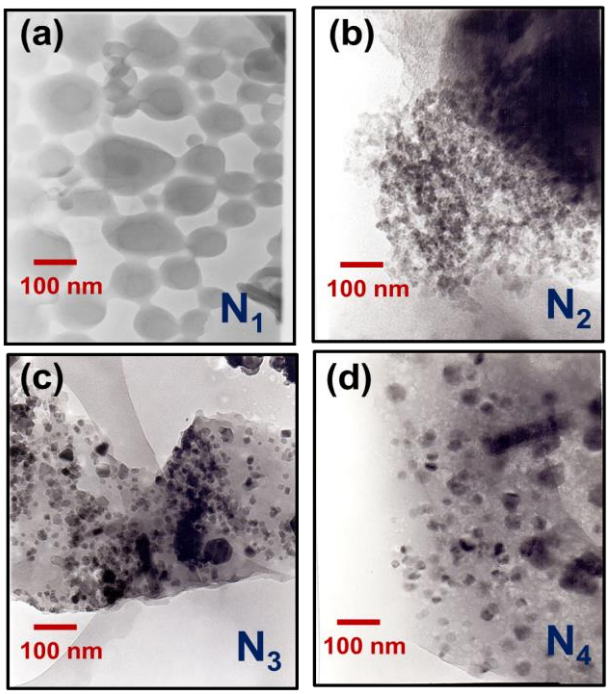

Figure 5.5: TEM micrograph for (a) Sample N_1 (b) N_2 (c) N_3 (d) N_4

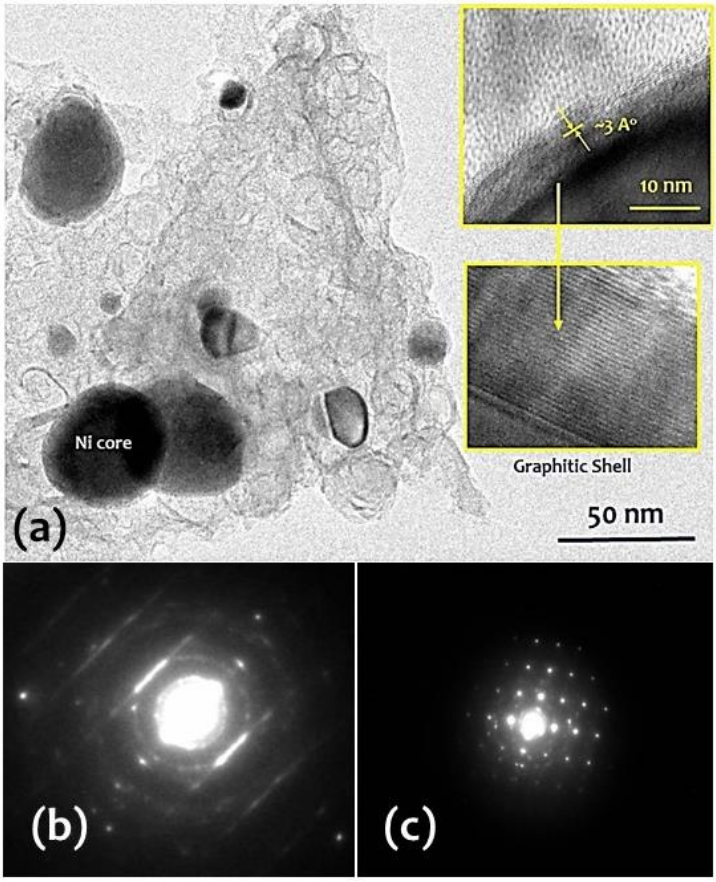

Figure 5.6: (a) HRTEM micrograph for sample N_4 (b) SAED pattern of Ni core (c) SAED pattern of graphitic shell

Further HRTEM studies are carried out on N_4 sample and results are shown in Figure 5.6(a). The Ni core is found to be nearly spherical in shape and its size is ~40 nm. Further, the shell structure is composed of onion like graphitic carbon layer, as shown in inset panel of Figure 5.6(a). The thickness of each graphitic carbon shell layer is found around ~3 A°, whereas the total shell thickness is found around ~ 7 nm. The Selected Area Electron Diffraction (SAED) pattern has been measured to understand the nature of metallic Ni core and graphitic shell materials and results are presented in Figure 5.6(b) and 5.6(c), respectively. The SAED patterns for Ni core metal shows concentric ring pattern, confirming the formation of polycrystalline Ni metals. However, the SAED pattern of graphitic shell shows bright spots indicates the formation of highly ordered crystalline layered graphitic carbon shells around Ni nanoparticles [Jeong *et al.*, 2008].

5.3.4 Raman Studies

Raman spectroscopy is one of the most confirmative techniques to identify the chemical bonding and microstructural details of carbonaceous materials. In the present study, Raman spectra were recorded in the range of 900-1800 cm^{-1} for the samples N_3 and N_4 and are shown in Figure 5.7(a) and (b), respectively. The broad peak observed for both the samples at ~ 1350 cm^{-1} is attributed to "disordered carbon" referred as D-peak and peak positioned at ~1580 cm^{-1} is appearing due to "graphitic carbon" known as G-peak [Roy *et al*., 2003; Ferrari, 2007]. The D-band (~1347 cm^{-1}) in these core-shell structure is slightly shifted towards the lower wavenumbers as compared to single crystal graphite (1360 cm^{-1}) and is consistent with reported literature [Zhang *et al.,* 2007; Liu *et al.*2010]. This shift is due to the confinement of phonons, originated from curvature and non-uniform distribution of graphitic layers with presence of lattice defects. Further, the intensity of D-peak (I_D) and G-peak (I_G) varies with annealing temperature for graphite coated Ni samples. The ratio of both the intensities (I_D/I_G) was calculated and found ~0.819 for sample N_3 and ~0.925 for sample N_4, confirming the formation of disordered/defected graphitic shell structure over Ni metal nano-core.

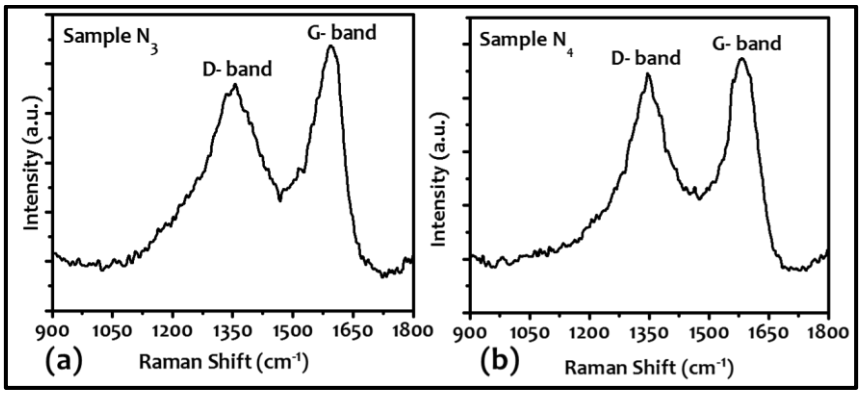

Figure 5.7: Raman spectra for sample N_3 and N_4

5.3.5 Magnetic Studies

Field dependent magnetization (M-H curve) were recorded for annealed samples N_2, N_3 and N_4, in 50 K-300 K temperature range and graphs are summarized in Figures 5.8(a)-(c). All the samples show ferromagnetic behavior in the recorded temperature range of 50-300 K due to the formation of Ni nano-metallic core. The saturation magnetization (M_s) has increased from ~12 to 24.3 emu/g for samples annealed at different temperatures from 550°C to 850°C i.e. N_2-N_4 samples.

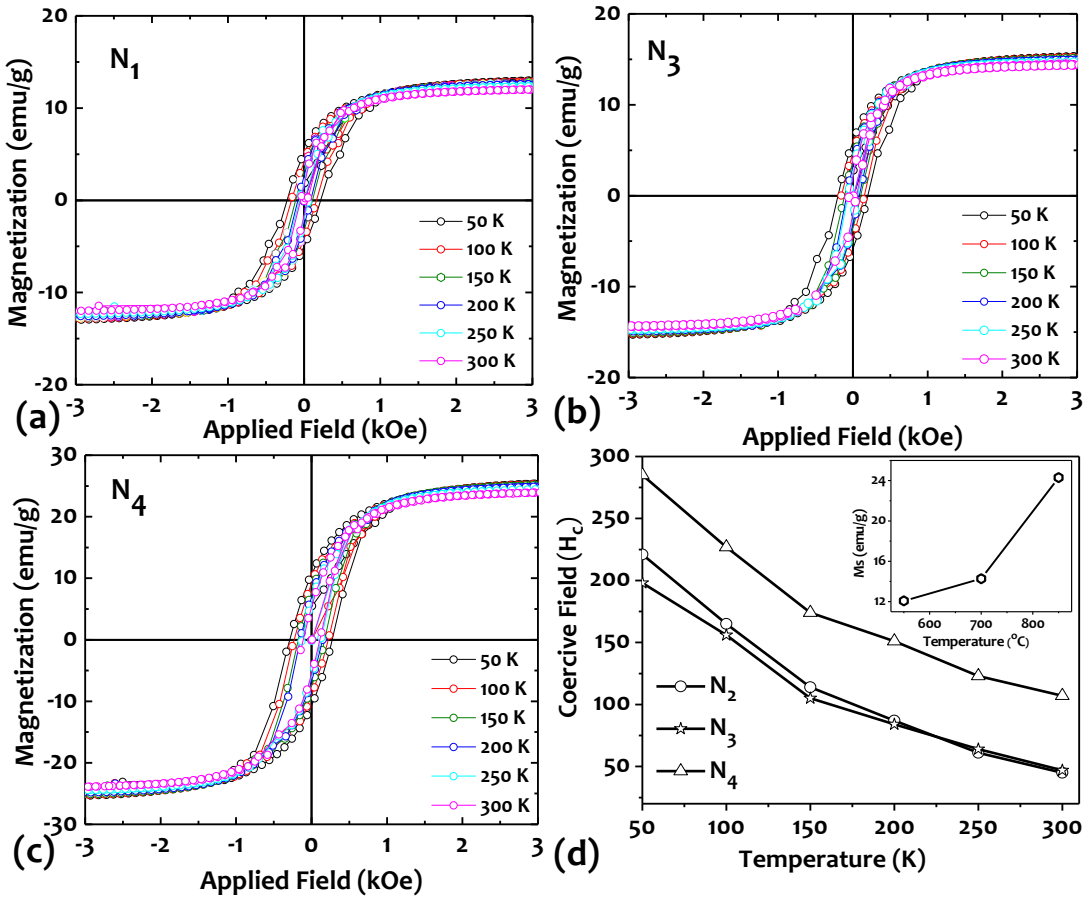

Figure 5.8: M-H hysteresis curves at different temperatures for graphite coated Ni nanomaterial samples (a) N_2 (b) N_3 (c) N_4 (d) Variation of coercive field H_c with cooling down of samples during magnetic measurements and variation of saturation magnetization in sample N_2-N_4

The increase in magnetization value is attributed to the growth of Ni metal particles with larger magnetic grains. However, presence of graphite shell on the surfaces affect the magnetic properties of core Ni metal significantly, as the measured saturation magnetization value (Ms ~24.3 emu/g) for 850°C annealed sample is still lesser than bulk pristine Ni (~55.4 emu/g). The

coercive field increases with lowering temperature from 300 K (RT) to 50 K for all the samples N_2-N_4. This effect may be attributed to freezing of spins while cooling the samples below room temperature, resulting into the irreversible spin movement locking because of the reduced thermal energy of Ni nanoparticles. The coercive field values for samples N_2 and N_3 are found almost similar with room temperature values ~ 45 Oe as shown in Figure 5.8(d), which is much lower than coercive field of bulk Ni (~176 Oe) [Saravanan *et al.*, 2001]. This observation suggests the room temperature superparamagnetic behavior for samples N_2 and N_3. The coercive field (H_c) value for sample N_4 has increased as compared to the other two samples, as summarized in Figure 5.8(d).

Temperature dependent magnetization studies were performed under external DC magnetic field of 500 Oe in the range of 5-350 K under zero-field-cooling (ZFC) and field- cooling (FC) conditions. The ZFC curves for all the samples are found broader in shape, indicating the formation of Ni nanoparticles with anisotropic particle size distribution [Bianco *et al.*, 2008]. When the samples are cooled from 350K to 5K without any external magnetic field, the random distribution of magnetic moment of each particle (or spontaneous magnetization) provides average magnetization in the samples. In the present case, the average spontaneous magnetization is ~ 6.5 emu/g for N_2, ~8.5 emu/g for sample N_3 and ~10.5 for sample N_4 (increases with sample annealing temperature due to presence of more aligned spins) as shown in Figure 5.9(a)-(c). In ZFC process, magnetization of each sample increases monotonously with heating from 5K to 300K, while external DC field is applied, due to overcoming of spin anisotropic energy supported by thermal energy provided to the system. The ZFC and FC curves for samples N_2 and N_3 are meeting each other nearby room temperature, which confirms that these samples retain their hysteresis behavior up to room temperature, as confirmed by M-H studies shown in Figure 5.9(a)-(b). The peak corresponding to maximum value of magnetization is at ~246 K for sample N_2 and ~251 K for N_3, which corresponds to their respective Blocking temperatures (T_B). Above T_B, both samples are showing superparamagnetic behavior, as magnetization values decreasing linearly with increase in temperature, as also supported by Figure 5.9(d) [Ji *et al.*, 2015]. The thermal excitations beyond T_B, provide way to overcome the energy barrier give rise to superparamagnetic behavior [Eisenmenger and Schuller, 2003].

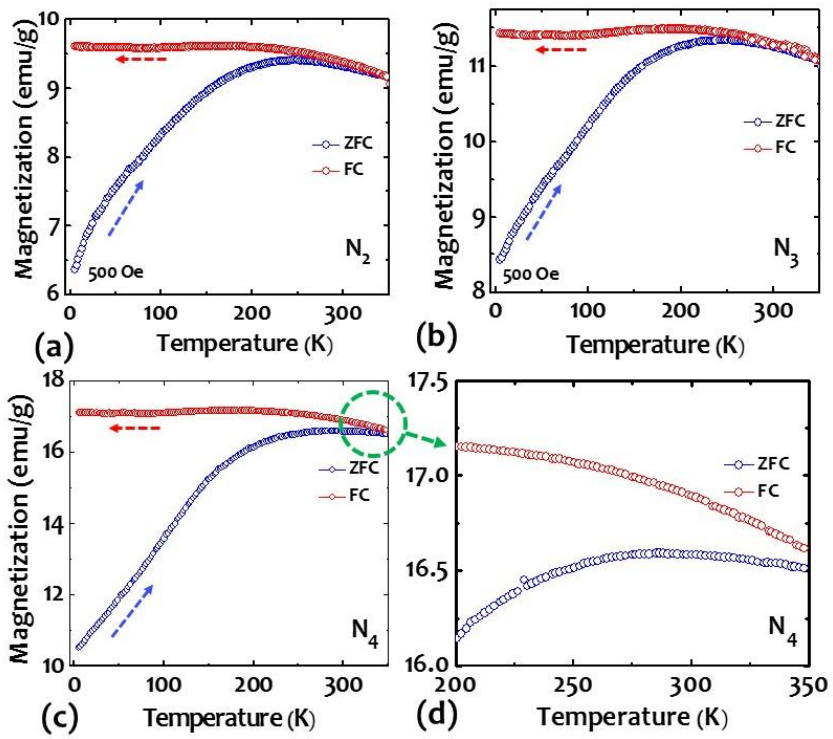

Figure 5.9: ZFC and FC magnetization curves for sample (a) N_2 (b) N_3 (c) N_4 in the temperature range 5-300K at applied magnetics field of 500 Oe

The ZFC and FC curves for sample N_4 are not meeting even up to 350 K and may meet at higher temperature. This confirms the strong ferromagnetic interaction in Ni nanoparticles in sample N_4 leads to high saturation magnetization, as also seen in Figure 5.9(d). Further, for all the samples N_2-N_4, the FC curves are having marginal increment with saturating trend, in field cooling conditions. This behavior arises due to core-shell structure of Ni and graphite layer. Under the influence of external magnetic field, the graphitic shell acts as pinning layer for spins present in Ni core metal, through exchange interactions. This pinning mechanism prevents the free rotation of spins contributed by Ni metal with external magnetic field resulting into saturation magnetization in the system [Roy *et al*., 2004].

5.3.6 Microwave Studies

Complex permittivity and permeability of graphite coated Ni nanomaterial samples were measured in Ku-band (12.4-18 GHz) microwave frequencies. The sample N_4 with highest value of saturation magnetization was selected for MW absorption studies. We could not measure complex permittivity and permeability of pure powder sample N_4 due to its highly conducting (electrical) nature of the sample. Therefore, rubber composites have been prepared by loading different concentration of powder (N_4) in rubber matrix to study the EM properties. MW characterizations of all rubber composites, NIBR40-NIBR75 (as listed in Table 5.1) are shown in Figure 5.10. The real part of permittivity (ε_r') for 40wt% loaded sample (NIBR40) is almost constant ~5.5 throughout the frequency range 12.4-18 GHz. The permittivity value has increased to ~8.5 with increase in the loading fraction of powder (NIBR50) and is nearly constant over Ku-band. However, beyond 50wt% loading fraction, the dispersion of ε_r' is showing decrease in the range ~11-14 for NIBR60, ~ 16-19 for NIBR70 and ~18-23 for NIBR75 composite samples as shown in Figure 5.10(a).

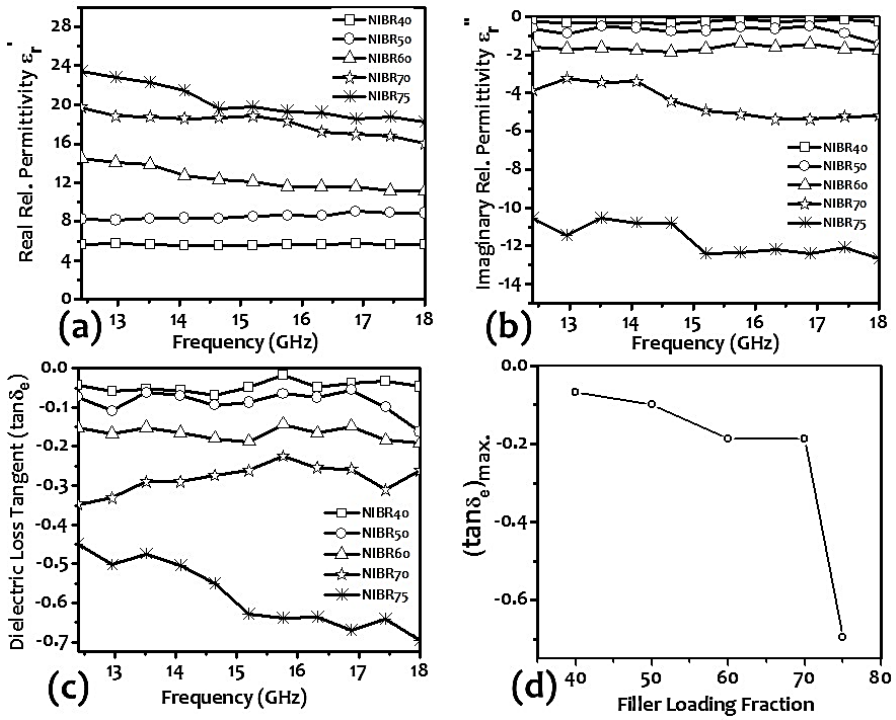

Figure 5.10 : Frequency dependent plots of different filler loaded rubber composites for (a) Real relative permittivity ε_r' (b) Imaginary relative permittivity ε_r'' (c) Dielectric loss tangent $\tan\delta_e$ (d) Variation of maximum loss tangent $(\tan\delta_e)_{max}$ with filler loading fraction of N_4 powder

The enhancement of ε_r' values with higher loading fraction is due to the increased quantity of functional material in rubber matrix, as given in Table 5.1. The variation of imaginary part of permittivity (ε_r'') with frequencies is shown in Figure 5.10(b). The values found to be ~ -0.25, ~ -0.65 and ~ -1.5 for NIBR40, NIBR50 and NIBR60 composites samples, respectively. For all these

composites, we have observed that ε_r'' is non-dispersive in the nature against frequencies. However, ε_r'' values have increased significantly in the range of ~ -3.25 to -5.30 for the sample NIBR70 in the frequency range of 12.4-18 GHz. On further increase in concentration of filler materials in NIBR75, ε_r'' values have increased drastically in the range of ~ -10.55 to -12.66 in the complete frequency band. The increased value of complex permittivity at higher loading of filler material resulted due to the increase in number of dipoles, causing relaxation for maximum dissipation/loss of MW signals. The real permeability (μ_r') for all the composite sample were observed ~1 with negligible contribution of imaginary part of permeability (μ_r''), indicating the absence of magnetic loss characteristics in these samples. Figure 5.10 (c) shows the variation of calculated dielectric loss tangent values ($\tan\delta_e = \varepsilon_r''/\varepsilon_r'$) with MW frequencies in the range of 12.4-18 GHz. For samples NIBR40 and NIBR50, loss tangent values are found ~ -0.05 and ~ -0.08, respectively. Similarly for sample NIBR60, $\tan\delta_e$ values increase significantly in the range of ~ -0.15 to -0.20 in frequency range 12.4-18 GHz. Loss tangent values for NIBR75 rubber composite found in the range of ~ -0.45 to ~ -0.69 over the entire range of 12.4-18 GHz. The high value of dielectric loss in higher loading composite samples may be attributed to the relaxation of space charge and dipolar polarization of large numbers of filler materials in the rubber matrix.

The thickness dependent calculated reflection loss (R.L.), for all the rubber based MW absorbers ranging NIBR40-NIBR75 over the frequency range 12.4-18 GHz using equation (4.2), are shown in Figures 5.11 (a)-(e). The 40 wt% loaded sample (NIBR40), has no significant MW absorption characteristics with R.L. values > -3 dB over Ku-band with maximum value $(R.L.)_{max}$ ~ -8 dB at ~15 GHz as shown in Figure 5.11(a). The optimized absorber thickness of this composite found to be ~6.4 mm. There is no significant increase in loss characteristics observed in 12.4-18 GHz with the increase in filler loading concentration for NIBR50. However, R.L. characteristics showed weak resonating behavior with enhanced absorber thickness and the resonating frequency is shifting towards lower frequency with increasing the absorber thickness. The maximum of R.L. values $(R.L.)_{max}$ found to be ~ -11 dB for 4.6 mm absorber thickness, which shifted towards lower frequency with absorber thickness, when increased from 4.6 mm to 5.4 mm (Fig. 5.11b). This observation indicates that there is a partial impedance matching for the absorber, wherein the interaction of filler materials in the host rubber matrix with EM wave is not adequate to give the maximum absorption. Figure 5.11(c) shows the R.L. characteristics for NIBR60 sample, showing similar loss characteristics without any significant improvement in return loss values. The sample shows $(R.L.)_{max}$ ~ -15 dB in Ku-band at different thicknesses of the absorber viz. 4.6, 4.8, 5.0, 5.2 and 5.4 mm. This absorber sample shows > 90% MW absorption and can be tuned within Ku-band by varying the absorber thickness. Interestingly, for NIBR70 sample enhanced MW absorption characteristics are observed, wherein functional filler materials inside the host rubber matrix played an effective role to reduce the absorber thickness. The observed $(R.L.)_{max}$ is ~ -48 dB at matching frequency of ~17 GHz with significantly lower absorber matching thickness of 1.0 mm with respect to the other composite samples with relatively lower filling fractions. The MW absorption for this sample can be tuned by using the desired ($\lambda_m/4$) thickness of sample for the proper impedance matching of incident electromagnetic radiation. However, at higher matching thickness, (R.L.) values decreased significantly towards lower frequency side with $(R.L.)_{max}$ ~ -33 dB at 1.1 mm, ~ -24 dB at 1.2 mm, ~ -20 dB at 1.3 mm and ~ -18 dB at 1.5 mm thicknesses. Thus, 1.0 mm thick composite NIBR70 sample may serve as a MW absorber for its application on targets where weight penalty is a serious concern in the Ku-band frequencies. The MW absorption properties of this composite at lower thickness is found promising as compared to other reported composite based on core shell structure [Zhang *et al*., 2006; Liu *et al*., 2010; Xie *et al*., 2011].

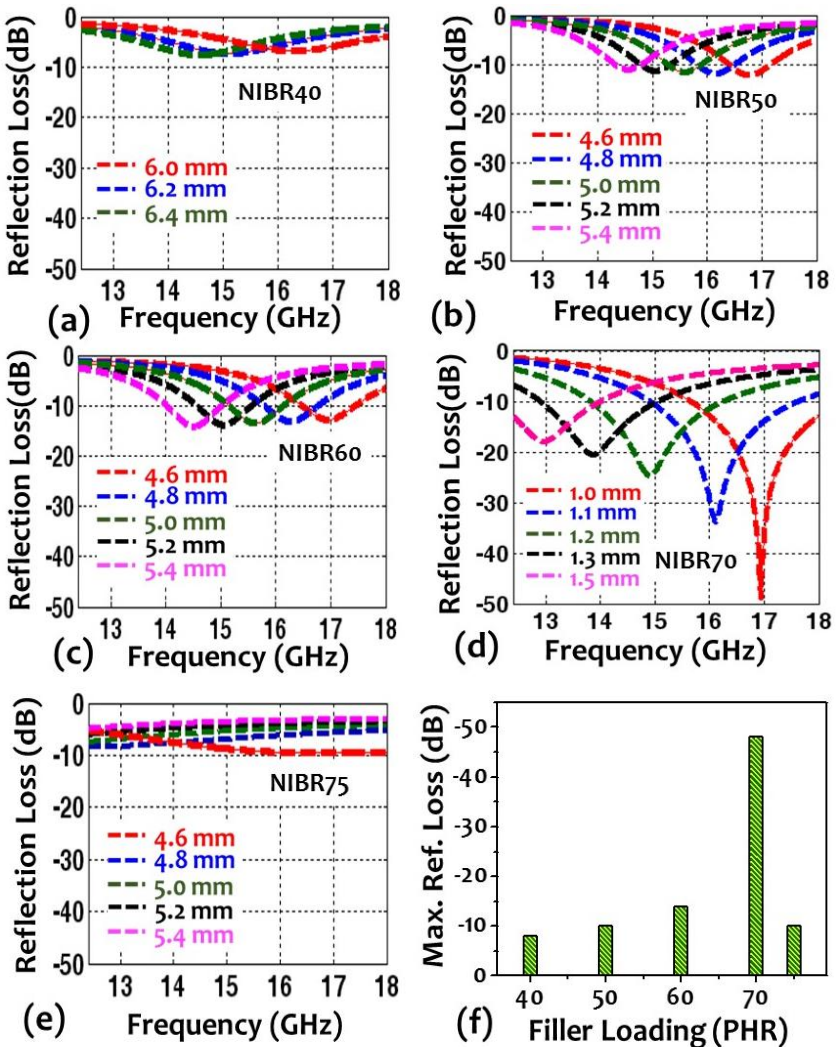

Figure 5.11: Optimal Reflection Loss (R.L.) over frequency range 12.4-18 GHz and matching thicknesses of N_4 powder loaded rubber composites (a) NIBR40 (b) NIBR50 (c) NIBR60 (d) NIBR70 (e) NIBR75 (f) Variation of maximum reflection loss with functional filler loading fraction in composites

In 75wt% loaded NIBR75 rubber composite sample, the reflection loss values reduced drastically in spite of the high loss tangent values in 12.4 - 18 GHz frequency range. The maximum values of R.L. $(R.L.)_{max}$ found ~ -8 to -10 dB at thickness 4.6 mm in the investigated frequency range. Further, the MW absorption was nearly frequency independent with relatively lower reflection loss values in the entire frequency band for larger thicknesses (Fig. 5.11e). This behavior of R.L. is attributed to the higher order of impedance mismatch between the incident MW radiation and the absorber surface for all absorber thicknesses. This suggests that even though large magnetic tangent losses are present in the material, the impedance matching at surface of absorber is important to get the optimal MW absorption characteristics. Therefore, as discussed in chapter 2, in conjunction with the high dielectric/magnetic loss properties of materials, impedance matching is an essential criterion for the design and development of MW absorbers. Figure 5.11(f) summarizes the trend of maximum R.L. values with increase in filler loading fractions and assists in selecting the suitable composite material for such applications.

5.4 CONCLUDING REMARKS

Synthesis of Ni hydroxide nanocomposite was carried out using a simple, energy efficient and scalable wet chemical route. Formation of Ni hydroxide within the copolymer matrix has been confirmed from X-ray diffraction (XRD) and FTIR studies. Thereafter, core-shell Ni nanoparticles consisting of Ni nano metallic core and graphitic carbon shell has been synthesized using pyrolysis of $Ni(OH)_2$ nanocomposite material under inert ambient conditions at different

elevated temperatures. XRD studies explained the evolution of cubic phase pure Ni nanoparticles along with graphitic carbon phase. HRTEM studies confirm the formation of core-shell nanostructures having metallic Ni core of size ~40 nm with 'onion' like graphitic shell of thickness ~ 7 nm. Raman spectroscopy studies further confirmed the disordered nature of the graphitic carbon shell. Low and room temperature magnetic studies explain the ferromagnetic behavior of Ni nanoparticles, obtained from different annealing temperatures. Saturation magnetization (M_s) of these materials increased with increase in annealing temperatures. Further, coercive field values also increased while cooling the samples from 300 K to 50 K. The rubber based composites were fabricated by impregnation of identified filler materials (850° C annealed nickel/graphitic carbon core-shell structured material) for different concentrations. The EM properties are evaluated and R.L. characteristics are computed for these composite samples at different absorber thickness. Among these composites, 70wt% filler loaded rubber composite with thickness t= 1.0 mm showed the maximum R.L. ~48 dB at ~17 GHz. The thickness of absorber is fairly less due to proper absorber surface impedance matching. This MW absorber material may be suitable for specific MW absorption applications, where weight penalty is a serious concern.

...